https://doi.org/10.26599/FRICT.2026.9441222

Research Article

Extremely enhanced the tribocorrosion behavior of L-DED CoCrNi multi-principal element alloy by in-situ alloying

Yudong An[1,2,3], Fenghua Su[1*], Jianfang Sun[1,2], Jibin Pu[2,3*]

[1] *School of Mechanical and Automotive Engineering, South China University of Technology, Guangzhou 510640, China*

[2] *State Key Laboratory of Advanced Marine Materials, Ningbo Institute of Materials Technology and Engineering, Chinese Academy of Sciences, Ningbo 315201, China*

[3] *Qianwan Institute of CNITECH, Ningbo 315336, China*

Corresponding Author *: Fenghua Su, Email: fhsu@scut.edu.cn.

Corresponding Author *: Jibin Pu, Email: pujibin@nimte.ac.cn.

Received: September 4, 2025; Revised: November 13, 2025; Accepted: January 26, 2026

Abstract

Reducing corrosion and wear has been a challenge to metal components in the marine environment for a long time. However, the problem of high cost and low efficiency hinder the discovery of new anti-tribocorrosion multi-principal element alloy (MPEA). This study reported a significant reduction in both wear and corrosion of single-phase CoCrNi MPEA through in-situ Laser-directed energy deposition (L-DED), that had

only half tribocorrosion rate than pre-alloyed samples. Further, structure evolution mechanism of in-situ samples was revealed under different scales and interaction mechanism of tribocorrosion was clarified in detail. The results show that in-situ samples had finer cells and higher microhardness due to solid solution strengthening and nano-precipitation strengthening. The higher $Cr_2O_3/Cr(OH)_3$ ratio, higher R_{ct}, and a lower I_{pass}, indicated a denser and more protective passive film of in-situ samples. Further, in-situ sample demonstrated superior tribocorrosion resistance which was mainly due to lower corrosion-intensified wear loss (W_C) value. Moreover, load intensified the material loss of interactions between wear (W) and corrosion (S). This work will provide breakthrough in the wear-corrosion trade-off of MPEA design and promote the application of anti-tribocorrosion MPEAs in marine equipment.

Keywords

Multi-principal element alloys, Laser-directed energy deposition, Tribocorrosion, Wear, In-situ alloying

1 Introduction

With the rapid development of technology, it is becoming more and more important to accelerate the exploration and development of marine resources. However, corrosion and wear are ubiquitous in the moving parts of marine engineering and seriously reduce the service life of equipment such as the hydraulic transmission system of ships and deep-sea submersibles, gear sets of tidal power generation and tidal turbines, and feeding parts in deep-sea mine cars [1]. Normally, tribocorrosion involves pure corrosion, pure wear, and the interaction between corrosion and wear [2]. Under the synergistic effects, the loss rate of material is much higher than that under pure corrosion or pure friction conditions, which constitute a huge challenge for marine material engineering [3,4].

Compared with traditional alloys (nickel-based alloys [5], stainless steel [6], copper alloys [7]), the new MPEA proposed by Yeh et al. [8] is composed of almost equal

atoms or a significant proportion of various main elements and has excellent mechanical performance due to high entropy [9,10]. The classic CoCrNi alloy has a single Face-Centered Cubic structure, short-range chemical, and lattice distortion [11,12], and has been widely studied with various processes [13–15]. The CoCrNi alloy prepared by arc-melting under argon atmosphere reached a yield strength of 350 MPa, ultimate tensile strength of 794 MPa and an elongation of 20% [16]. Ren et al. [15] successfully prepared CoCrNi MPEA with Arc Melting, the result shows that low Stacking fault energy (SFE), high lattice friction stress, and chemical short-range order (CSRO) provide additional strengthening and toughening, thereby significantly improving the wear resistance under low temperature. In addition, the slow diffusion effect in CoCrNi has a beneficial effect on the high-temperature performance and exhibits higher oxidation resistance than CoCrFeMnNi and SS 304 [14]. Dong et al. fabricated CoCrNi alloy by using plasma arc melting, and the sample showed excellent oxidation resistance and corrosion resistance [17]. CoCrNi prepared by LPBF showed high strength and high toughness [18]. Ma et al. [19] synthesized CoCrNi MPEA with a wear rate of 3.8×10^{-5} $mm^3N^{-1}m^{-1}$ and corrosion current density of 2.7×10^{-6} A/cm^2 by spark plasma sintering. Obviously, under different preparation processes, the microstructure formation process of CoCrNi alloy is different, which will lead to different properties of the alloy.

As a revolutionary technique, Laser-directed energy deposition (L-DED) has significant advantages in complex structural component manufacturing [20–22]. By melting and solidifying metal powders, metal components are built layer by layer to manufacture equipment parts with various complex shapes. Recent studies have demonstrated that L-DED can successfully produce MPEAs with controllable microstructures and excellent performance characteristics [23–26]. Melia et al. [27] successfully prepared low-porosity, high-strength, and high-ductility bulk CoCrFeMnNi parts through the L-DED process. However, L-DED requires alloy powders with good fluidity [28] as raw materials, and has strict requirements on powder preparation techniques [27], powder humidity[29], particle morphology [30], size distribution [31], sphericity [32], oxygen content [33], and composition [34]. Therefore,

the high cost, low success rate, and low efficiency of preparing alloyed spherical powders have hindered the development of new MPEAs suitable for additive manufacturing. Although pre-alloyed powders can be replaced by mechanical mixing of single powders, the effect about different powder pre-alloyed forms on structure of additive manufactured MPEA is still unclear. Due corrosion and wear have been a challenge to metal components in the marine environment, and the material loss rate during tribocorrosion is much higher than that under pure corrosion or pure friction conditions. There are few reports on how the in-situ alloying influences the mechanical properties and marine protection properties of MPEA.

Herein, CoCrNi alloy was successfully prepared by using pre-alloyed powder and mechanically mixed powder, and the influence of in-situ about microstructure, anti-corrosion, and tribocorrosion behavior was invested. The microstructure of different samples was studied by using characterization techniques, and the above conclusions was combined with the of electrochemical and tribocorrosion results. The synergistic effect between wear and corrosion was quantitatively calculated. Finally, the intrinsic reasons for in-situ alloying on microstructure and protective properties of MEPA was obtained. This work will provide breakthrough in the wear-corrosion trade-off of MPEA design and promote the application of anti-tribocorrosion MPEAs in marine equipment.

2 Experiments

2.1 materials and preparation

Co, Ni powder with particle size of 50-150 μm, Cr powder with particle size of 15-45 μm (considering that Cr has the highest melting point, a smaller particle size was used), and CoCrNi pre-alloyed powder (Co:Cr:Ni=1: 1: 1, 50-150 μm) were used as raw materials. The microstructure and particle size of different powders were shown in Fig. S1. The samples were prepared by using an ACunity directed energy deposition system equipped with KUKA robot, Oerlikon powder feeder, Laser-Line laser system, and ACunity coaxial nozzle. Argon (purity⩾99.999%) was used as powder carrier gas and shielding gas in the L-DED process. As shown in Fig. 2, powder blend was mixed in

an Al_2O_3 tank by using a ball mill for 2 h. The typical process parameters were: laser power of 850 W, deposition rate of 10 mm/min, a hatch spacing of 0.8 mm, overlap rate of 60%, shielding gas flow of 14 L/min, carrier gas flow of 5 L/min, and spot diameter of 2 mm. Each cladding layer was clad in a reciprocating manner, and the cladding direction was rotated 90° between layers. The sample dimensions were 45×45×25 mm.

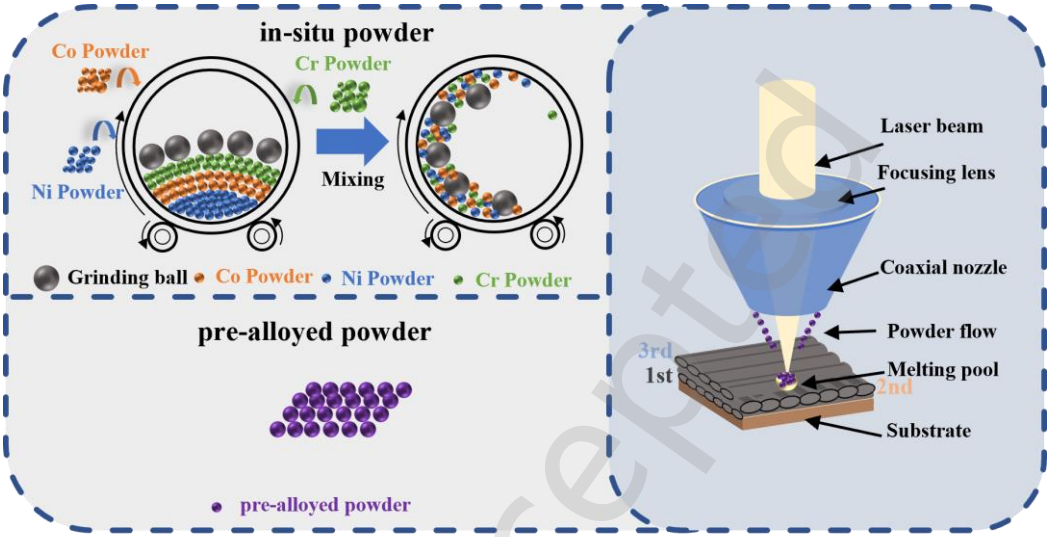

Fig. 1 The diagram of the L-DED process.

2.2 Characterizations

Samples were ground with SiC emery paper, and polished with 0.5 μm diamond suspension solutions, aqua regia was used to etch the sample. An X-ray diffractometer (XRD, ADVANCE D8) with Cu-Kα radiation was used to characterize phase of samples, the scanning range was 30◦-100◦, scanning speed was 5◦/min, and a step length was 0.02◦. The scanning electron microscope (SEM, GeminiSEM300) equipped Bruker EBSD detector, and optical microscope (OM, Axio Observer 5) were used to observe the microstructure. and the AZtecCrystal software was used to process images. Further, the Electron Probe X-ray Micro-Analyzer (EPMA, JXA-iHP200F) was taken to value the elements distribution. The X-ray photoelectron spectroscopy (XPS, Axis Ultra DLD) was used to characterize passive film. The TEM samples were processed by double-jet electropolishing technique and observed by transmission electron microscopy (TEM, Talos F200x). The microhardness was valued with a microhardness tester (VH3300), the load was 0.02 kg, and time was 10 s.

2.3 Corrosion and tribocorrosion tests

A three-electrode electrolytic cell and electrochemical workstation (Autolab PGSTAT302N, Metrohm) were used to perform electrochemical experiments. The sample was working electrode with an area of 1 cm^2. A platinum sheet was used as the counter electrode, and an Ag/AgCl electrode was used as the reference electrode. Firstly, a potentiostatic polarization (PS) at -1 V for 200 s was tested to remove the oxide film, followed by open circuit potential (OCP) for 3600s, and electrochemical impedance spectroscopy (EIS) was tested. The test parameters were frequency range of 100000-0.01 Hz and AC signal interference of 10 mV. Subsequently, a Potentiodynamic polarization (PD) test was performed at -0.1-1.5 V (vs OCP), the scan rate was 1 mV/s. All experiments were tested with 3.5 wt% NaCl solution at room temperature to simulate seawater environment.

Tribocorrosion tests were carried out by using a friction tester (UMT TriboLab) with homemade liquid cell and linear reciprocating sliding mode (Fig. 2). The loads were 1, 5, and 9 N, the sliding distance was 3 mm with friction frequency of 2 Hz and time of 30 min. The grinding ball was Si_3N_4 with a diameter of 4.5 mm. During the process, the Ag/AgCl electrode was the reference electrode and the Pt electrode was the counter electrode. Three types of tribocorrosion experiments were carried out as below:

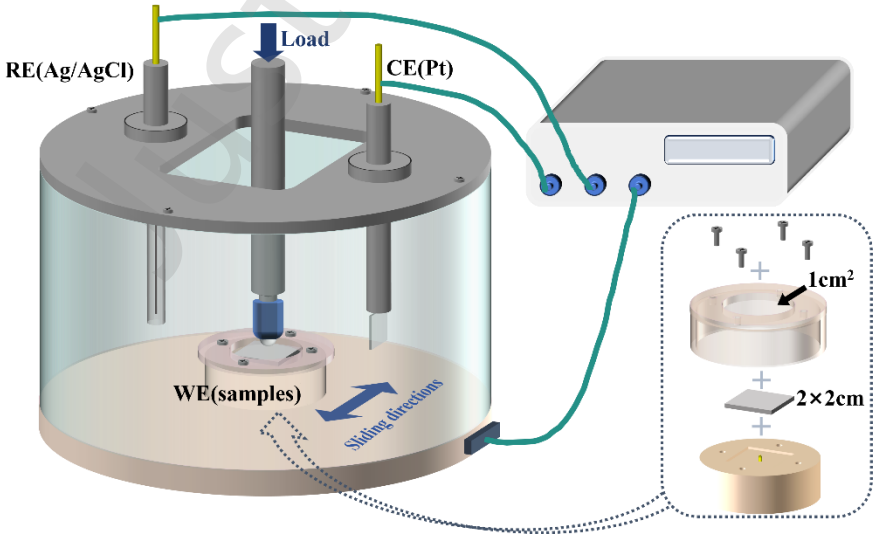

Fig. 2 The schematic of the tribocorrosion process.

(1) Open circuit potential conditions: After the sample was immersed in the solution, the OCP was recorded for 4800 s and the friction time was 1800 s.

(2) Potentiodynamic polarization conditions: After the sample was immersed in the solution for 30 min, a PD scan was performed at -0.1-1.5 V (vs OCP), 1 mV/s, and the friction coefficient was recorded at the same time.

(3) Cathodic protection conditions (-0.9 V, vs RE): The cathodic protection condition was taken to eliminate the impact of corrosion during friction, the friction conditions were consistent with the OCP conditions. All experiment for each sample was repeated at least 3 times.

The worn surface morphology was valued by laser confocal microscope. The wear rate was calculated by the formula (1):

$$W = \frac{V}{F \cdot L} \tag{1}$$

Where W is the wear rate ($mm^3 \cdot N^{-1} \cdot m^{-1}$), V is the total friction corrosion volume (mm^3), F is the applied load (N), and L is the total sliding distance (m).

Tribocorrosion is a degradation process of bonded materials associated with corrosion, wear, and synergistic effects. The total volume loss during tribocorrosion is calculated by using the following formula:

$$T = W_0 + C_0 + S \tag{2}$$

The total volume loss(T) is equal to the pure corrosion loss, the pure mechanical wear loss(W), and the interaction loss(S).

$$W = W_0 + W_C \tag{3}$$

Where W_0 is the pure wear loss in the absence of corrosive media, Wc is the loss caused by wear due to corrosion.

$$S = W_C + C_W \tag{4}$$

The additional loss caused by friction-corrosion interaction is consists of corrosion-intensified wear (W_C) and wear-intensified corrosion (C_W) [35,36].

$$C_0 = \frac{M \times I_2 \times t}{n\ F\ \rho} \tag{5}$$

$$C_W = \frac{M \times (I_2 - I_1) \times t}{n\ F\ \rho} \tag{6}$$

Where I_2 is corrosion current under static conditions. I_2-I_1 is the difference in corrosion current measured between sliding and no sliding [35]. t is sliding time, F is the Faraday constant, ρ is the density of the alloy, M is the atomic mass of the metal, and n is the number of charges involved in the oxidation reaction.

3 Results and analysis

3.1 Initial microstructures

Fig. 3 showed the typical microstructure of L-DED CoCrNi alloy prepared by pre-alloyed powder. The pre-alloyed sample had obvious anisotropy along different planes and obvious molten pool boundaries. Further, traces of the molten pool gradually accumulated layer by layer were shown in the XZ plane, which was owing to the cladding direction rotating 90° between adjacent depositions during the cladding path design process. The L-DED samples in the XZ plane show an uneven grain size distribution and obvious molten pool characteristics due to the high cooling rate (Fig. 3 (d)), the equiaxed cells mainly appeared inside the molten pool, while columnar cells appeared at the bottom of molten pool (Fig. 3 (e, e1, e2)).

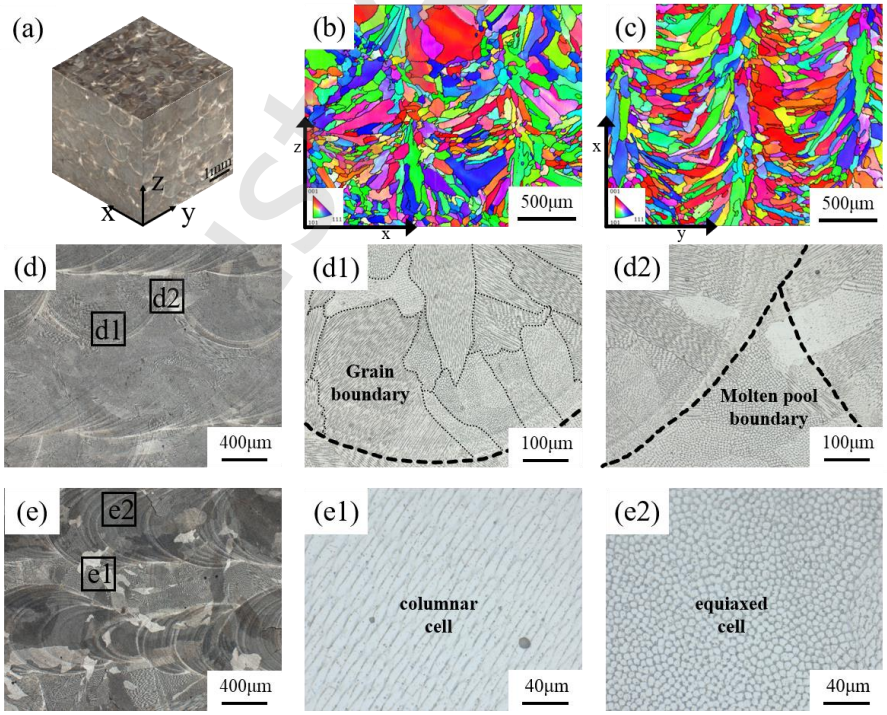

Fig. 3 The microstructure of pre-alloyed samples at different areas: (a, d, e) the OM image; (b, c) the EBSD image.

Fig. 4(a) showed the phase composition of different samples and powders. Both samples and pre-alloyed powder had a typical FCC structure, and the diffraction peaks of all samples were (111), (200), and (220). In addition, the (111) peak of the pre-alloyed samples were stronger than that of the powder and In-situ samples. Pre-alloyed samples had preferred growth orientation on the (111) crystal plane.

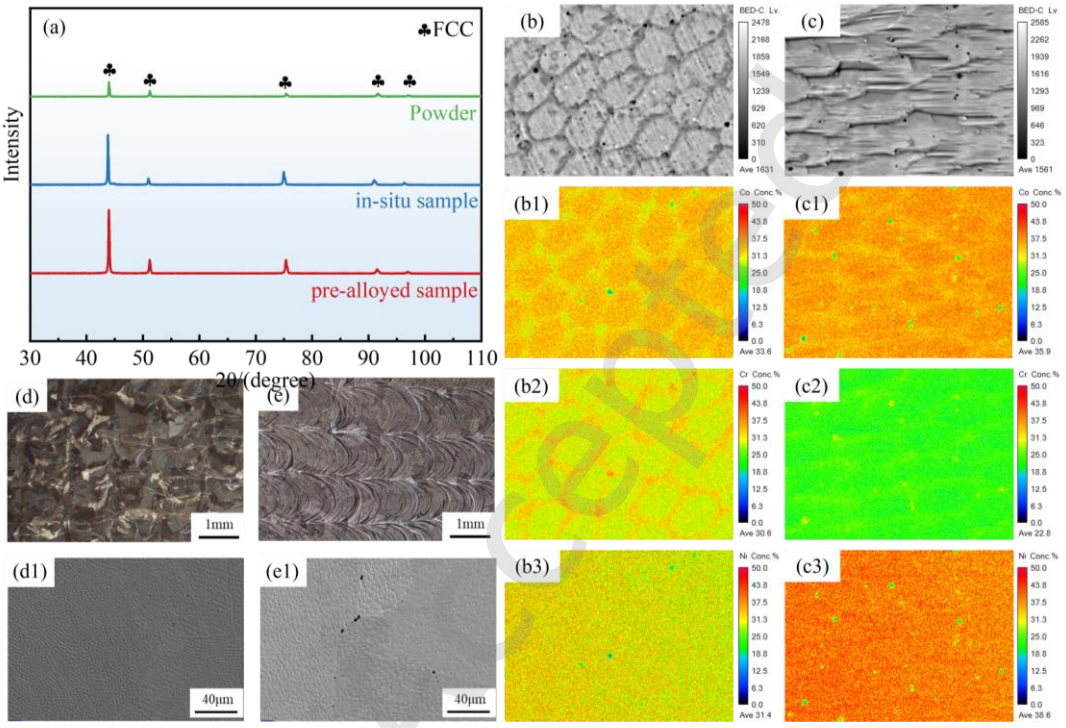

Fig. 4 The microstructure and phase of different samples: (a) the XRD patterns of powder and different samples; The EPMA maps of (b, b1, b2, b3) pre-alloyed samples and (c, c1, c2, c3) in-situ samples; the microstructure of (d, d1) pre-alloyed samples and (e, e1) in-situ samples.

Fig. 4 (d, d1) and Fig. 4 (e, e1) were surface microstructures of the pre-alloyed sample and in-situ sample, respectively. At low magnification (Fig. 4(d, e)), the grains of different orientations in the pre-alloyed samples had very obvious characteristics. However, a very obvious fish-scale molten pool feature appeared in the in-situ sample which may be due to the different melting points of different powders during the solidification process of the in-situ sample. At high magnification, the surface structure of both samples was equiaxed cells (Fig. 4(d1, e1)). In addition, the EDS results show that there was a segregation of Co and Cr elements within and between the cells in the

in-situ sample (Fig. S2). Fig. 4(b, c) showed the EPMA image of the sample surface. The composition of Co, Cr, and Ni in the pre-alloyed samples was roughly the same as the composition of the powder, while the element content of in-situ samples was different from the pre-designed composition. Which may be caused by the melting point difference between Co, Cr, and Ni powder. Both samples had Co and Cr segregation within and between the cells, with Co enriched within the cell and Cr enriched at the cell boundaries. The segregation phenomenon of the pre-alloyed samples was stronger than that of the in-situ samples.

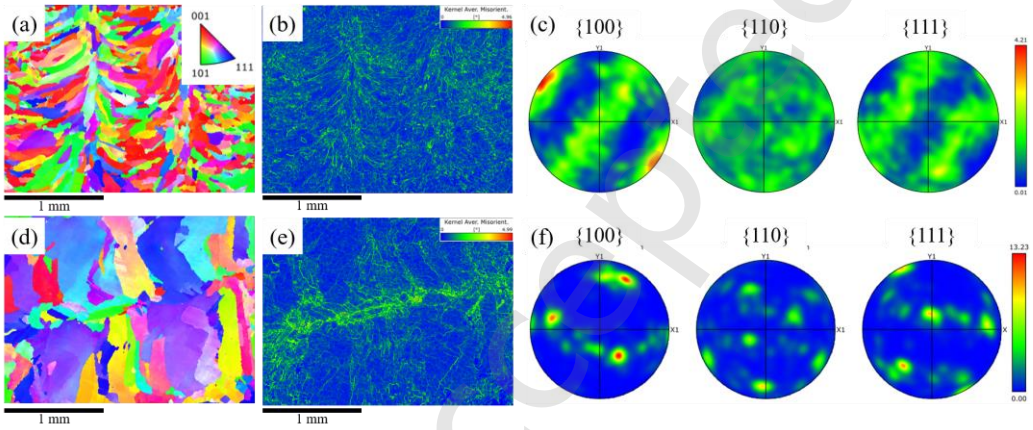

Fig. 5 The EBSD map of (a-c) pre-alloyed samples and (d-f) in-situ samples: (a, d) IPF; (b, e) KAM; (c, f) pole figures.

Besides the cell zones differences, there also were significant disparities in grain zones. Fig. 5 showed the EBSD results of the pre-alloyed samples and the in-situ samples, including inverse pole figure (IPF), kernel average misorientation (KAM), and pole figures. The pre-alloyed sample had a relatively irregular grain morphology and presented a complex orientation distribution. The grain growth direction was parallel to the heat flow direction during the melting and deposition process, showing a classic molten pool morphology. The grain morphology of the In-situ sample was relatively regular, and some grains were larger. Grain refinement was also shown in the adjacent overlapping area. In addition, the pre-alloyed sample had a higher KAM value, especially near the grain boundary, showing a significant misorientation gradient, which was related to the accumulation of dislocations generated during the pre-alloyed process. The KAM of the in-situ sample was mainly concentrated in the overlapping area. The

pole figures showed that the texture of the alloyed samples was weak and the orientation distribution was more random. The pole figures of In-situ samples showed a stronger preferred orientation, especially in the {100} direction, where the high strength points were more concentrated. The maximum orientation density of in-situ samples was higher (13.23) than that of pre-alloyed samples (4.21).

In summary, the pre-alloyed samples had refined and more irregular grains, and the dislocation accumulation near the grain boundaries was more serious. The in-situ samples had more regular grains. Further, the dislocations accumulate at the grain boundaries and cladding overlap areas, and the preferred orientation of In-situ samples was more obvious.

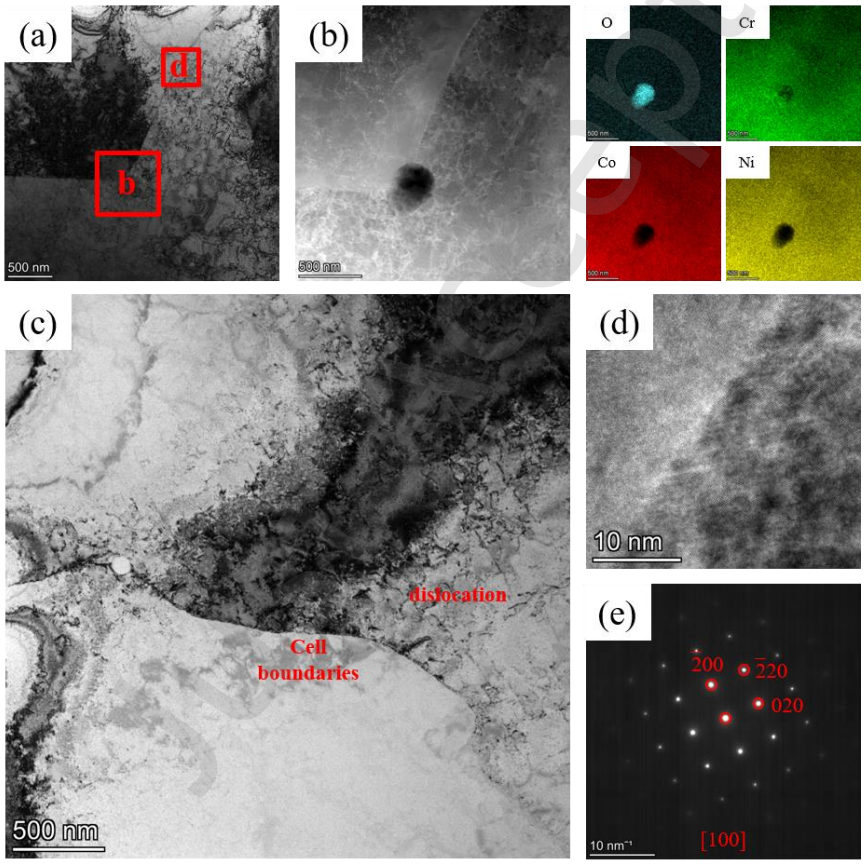

Fig. 6 The TEM of in-situ samples: (a, c) TEM images; (b) HAADF image; (d) HRTEM image; (e) SADP image.

To further elucidate the cell structure and matrix of the sample, TEM analysis was used to observe the in-situ samples. Obvious intergranular features and information about the existence of dislocations was observed in fig. 6(a, c). Further, according to the HAADF image (fig. 6(b)), there were some nano-scale oxide particles in the In-situ

sample, which were mainly concentrated in the intergranular area. This may be due to the Co, Cr, and Ni single powders had different melting points, and a few powders were melting and oxidized under the action of the laser, then tiny oxide particles entered into the molten pool and solidification into the intergranular area during the cell nucleation and solidification. In addition, according to the selected area diffraction pattern (SADP) image from (fig. 6(e)), the In-situ sample along the [100] zone axis exhibited a typical disordered FCC structure, which was consistent with the previous XRD results.

According to the Ellingham diagram, the Gibbs free energy of Cr_2O_3 formation remains significantly more negative than that of CoO or NiO across all relevant temperatures, indicating that Cr possesses a much stronger oxygen affinity than Co and Ni [37]. This thermodynamic tendency suggests that chromium oxide formation is more favorable under both storage and processing conditions. During L-DED, these oxides undergo dynamic evolution through a solid solution–reprecipitation mechanism [38]. Specifically, metal-oxygen bonds partially dissociate within the molten pool, and upon solidification, new metal-oxygen complexes re-form while being redistributed by Marangoni convection. This process allows nanoscale oxides to be uniformly dispersed in the matrix despite their density mismatch. As solidification proceeds, surface tension drives the consolidation of these oxides into regular-shaped inclusions that solidify together with the metallic matrix.

Fig. S3 showed the microhardness results of different samples. The average hardness of the pre-alloyed sample was about 245 $HV_{0.2}$, while the hardness of the in-situ sample was about 319 $HV_{0.2}$. The introduction of microstructural heterogeneity is one of the mechanisms for strengthening MPEA alloys [39]. The organization in the pre-alloyed sample is more uniform, while the in-situ sample has an inhomogeneous microstructure due to the uneven composition. In addition, nano-metal-oxides are used as a strengthening phase, and the particles hindered the movement of dislocations, thereby increased the hardness of the material. Ultimately, the synergistic strengthening led to a relatively high microhardness of the In-situ sample.

3.2 Electrochemical corrosion results

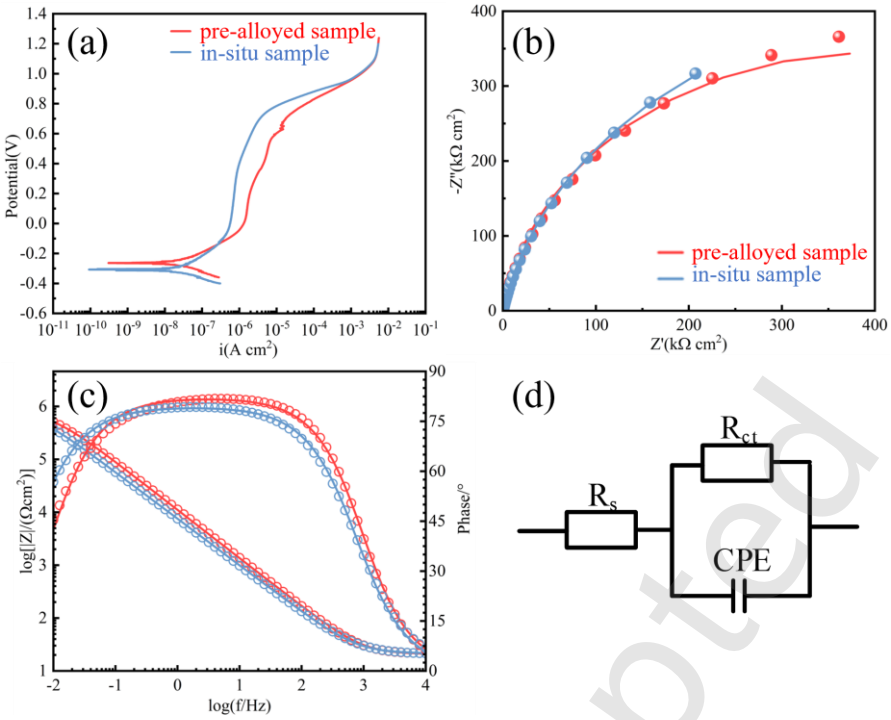

Fig. 7 The electrochemical performance of different samples: (a) Potentiodynamic polarization plots; (b) Nyquist plots; (c) Bode plots; (d) The equivalent circuit model.

Table 1. The fitting results of various samples.

Samples	E_{corr} (V)	I_{corr} (nA/cm^2)	I_{pass} μA/cm^2	R_s (Ω cm^2)	Q (μF/cm^2)	n	R_{ct} (Ω cm^2)
pre-alloyed	-0.2638	29.85	3.5371	20.84	16.86	0.9127	789500
in-situ	-0.3124	30.73	0.9775	21.3	26.17	0.8828	952900

The electrochemical experiments were obtained to distinguish the anti-corrosion proprieties of different samples (Fig. 7). Obviously, each sample showed obvious passivation process behavior. In addition, the in-situ sample had a wider passivation zone and a smaller I_{pass} of 0.9775 μA/cm^2. The E_{corr} and I_{corr} value was further obtained by the *tafel* extrapolation method. Both samples had similar I_{corr}, but the pre-alloyed sample had a higher E_{corr}. In summary, due to the heterogeneous structure caused by uneven element distribution, the in-situ samples had a lower corrosion potential and therefore had a higher corrosion tendency, the in-situ sample had a lower I_{pass} during

the passivation process, which indicates that the sample has formed a better passivation film.

Further, EIS results show that the Nyquist plots of both samples were typical semicircular arcs, which is due to a large amount of charge transfer occurring at the interface between the solution and the alloy. Generally, the arc size of the Nyquist plot can well reflect the impedance of the alloy passive film, and the impedance of the passivation film is positively correlated with the size of the arc diameter. The equivalent circuit was shown in Fig. 7(d), where R_s was the solution resistance. CPE was double-layer capacitance. R_{ct} was the charge transfer resistance. The R_{ct} of two samples were in the same order of magnitude, but the value of the in-situ sample was higher, indicating that the anti-corrosion performance about its passive film was higher, which was consistent with the potentiodynamic polarization results.

The constant phase angle element Q was Calculated by the following formula[40]:

$$Z_{CPE} = \frac{1}{Q(\omega j)^n} \ (-1 \le n \le 1) \qquad (7)$$

In which Y_0 represents proportional factor, j represents imaginary, ω represents frequency, and CPE is pure capacitance.

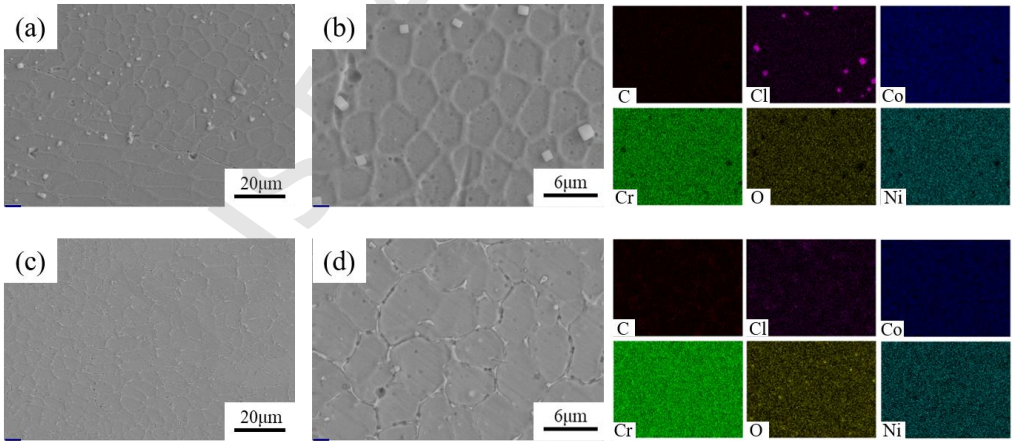

Fig. 8 The sample surface after the PD test: (a, b) pre-alloyed samples; (c, d) in-situ samples.

Fig. 8 showed the surface morphology of different samples after the potentiodynamic polarization test. All the samples surface showed morphological characteristics similar to the prepared metallographic state. Both CoCrNi samples were corroded, and dissolved along the cell intragranular and cell boundaries, further, the dissolution along

grain boundaries was also found. According to the EPMA results in Fig. 4(b, c), there was a typical Co, Cr element segregation phenomenon in the cell and cell boundaries of L-DED samples, which leads to the characteristics of local corrosion behavior. In addition, due to the relatively uniform distribution of Cr elements between the in-situ cell was smaller than that of pre-alloyed samples, the in-situ samples had smaller corrosion depth difference between cell and cell boundaries.

After samples were immersed in 3.5 wt% NaCl solution for 24 h, the XPS test was used to characterize the passive film. The fine spectra of O_{1s}, $Cr2p_{3/2}$, $Co2p_{3/2}$, and $Ni2p_{3/2}$ were respectively shown in Fig. S4, Fig. S5. Where Co was consisted of Co [41] and Co_3O_4 [42], Ni was consisted of Ni, NiO, and $Ni(OH)_2$ [43]. Cr was consisted of Cr [44], Cr_2O_3 [45] and $Cr(OH)_3$ [46]. The two samples had similar spectral characteristics. Co and Ni had the highest metal peaks, while oxide and hydroxide peaks of Cr were the highest, which means that the passive films of both samples were mainly composed of oxidized Cr_2O_3 and hydroxide $Cr(OH)_3$. Extensive studies have shown that Cr oxide and hydroxide are the main components of the passive film [47], and the relative concentration of Cr played a vital role in determining the anti-corrosion performance. Further, trace amounts of Co and Ni were observed in the passive film. The amount of NiO oxide formed in the passive film was minimal, which was attributed to the excellent oxidation resistance of Ni [48]. A dissolution of Co and Ni elements occurred during the formation of passive film compared with matrix alloy components. The analysis data were in good agreement with Cast CoCrNi [49]. The Co oxide and hydroxide present in the passive film are generally considered to have ionic and electronic conductivity, making it difficult to effectively protect the alloy matrix [50]. Therefore, the wider passivation zone and excellent local corrosion resistance of single-phase MPEA are mainly attributed to the high content of Cr_2O_3 present in passive film. Besides, related studies also showed that the selective dissolution mechanism of Ni can promote the formation of chromium oxide and chromium hydroxide in the passive film [51], and the reaction process is as follows. NiO and $Ni(OH)_3$ can also stabilize the passive film [52].

$$2Ni_xCr + 3H_2O \rightarrow 2xNi^{2+}(aq) + Cr_2O_3(s) + 6H^+ + (6+4x)e^- \quad (8)$$

$$Ni_xCr + 3H_2O \rightarrow 2xNi^{2+}(aq) + Cr_2OH_3(s) + 3H^+ + (3+2x)e^- \quad (9)$$

The contents of different components in the passive film were further calculated (Fig. 9). The contents of Co oxide and Co hydroxide in both samples were relatively close. The passivation film on the surface mainly consists of oxides and hydroxides, such as Co_3O_4, Cr_2O_3, and NiO, with extremely low metal content. However, with increasing etching depth, the O content in the coating significantly decreased, while the contents of elemental Co, Cr, and Ni gradually increased. Furthermore, the content of metal oxides gradually increased, while the content of metal hydroxides gradually decreased. Notably, the Cr content on the inner side of the passivation film was significantly higher than that on the outer surface. Finally, after prolonged etching, the composition became close to that of the metal coating. Overall, these results indicate that although both samples formed oxide passivation films, there are differences in the composition and stability of the passivation films. The contents of nickel oxide and nickel hydroxide in the in-situ sample were significantly reduced, and the content of cobalt oxide was also significantly reduced. The protective performance of the passive film can be further evaluated by calculating the ratio of $Cr_2O_3/Cr(OH)_3$ [53,54]. The increase in $Cr_2O_3/Cr(OH)_3$ ratio led to a better barrier property. The in-situ sample had a higher $Cr_2O_3/Cr(OH)_3$, indicating that passive film on in-situ samples had better corrosion resistance. The above result was consistent with previous EIS results.

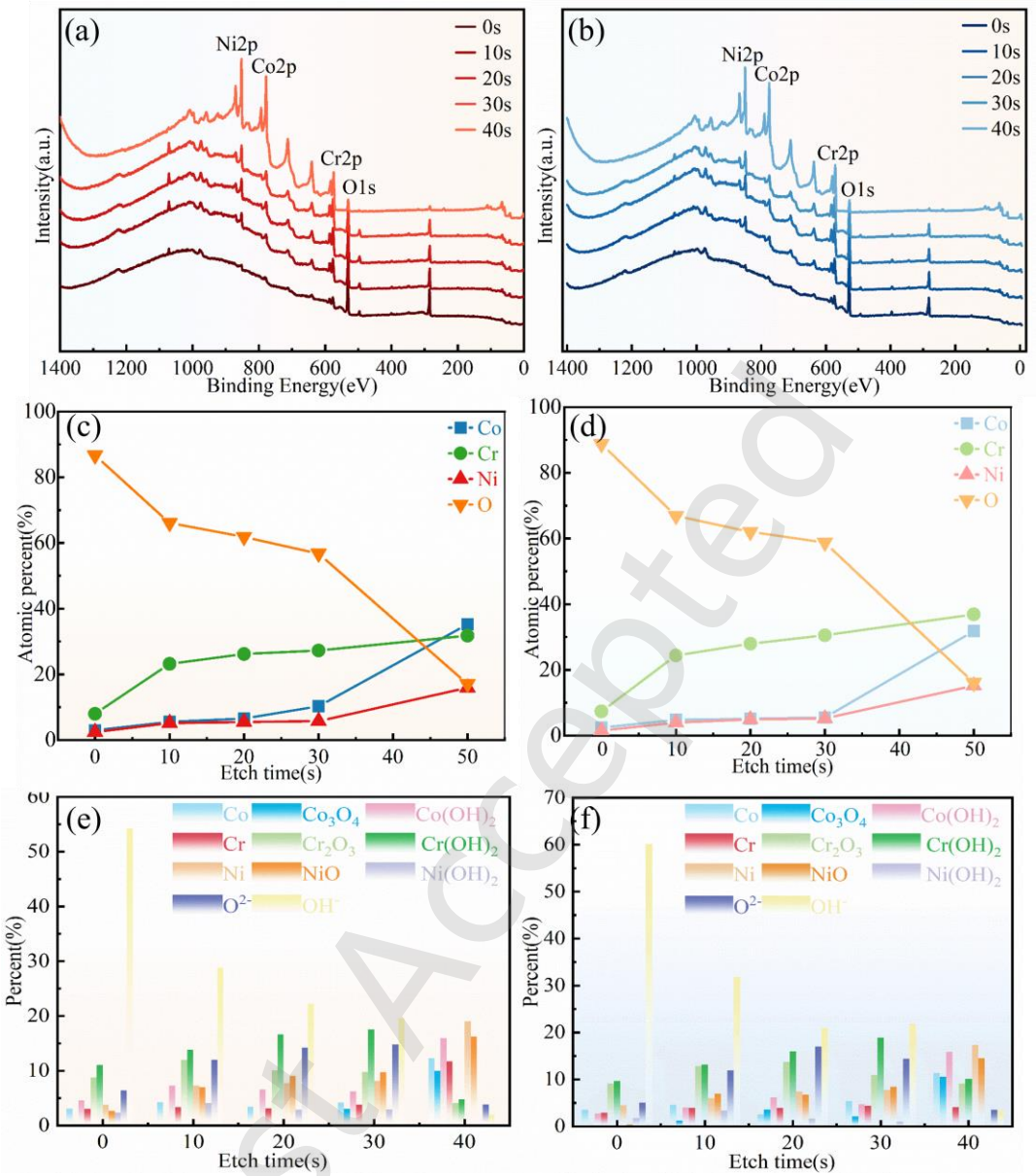

Fig. 9 The XPS results of pre-alloyed sample (a, c, e) and in-situ sample (b, d, f): (a, b) XPS full scan spectrum; (c, d) Atomic fraction summary; (e, f) Different valence ions content in the passivation film.

3.3 Tribocorrosion behavior

Fig. 10 (a, b) showed the OCP of samples before, during, and after tribocorrosion. As friction started, passive film was scratched, resulting in wear scars and OCP suddenly dropped. While the OCP gradually returned to the initial potential as friction ended. The potential of the metal during friction should theoretically correspond to its thermodynamic equilibrium potential, which was usually much lower than the open

circuit potential. Therefore, the OCP observed during friction was caused by the galvanic couple established between de-passive and passive areas [55]. The OCP changes of samples during the tribocorrosion process were discussed in detail as follows. The OCP of both samples showed a gradual stabilization phenomenon. However, the OCP of both samples under 1 N and 5 N loads first increased and then gradually decreased and stabilized, while the OCP under a load of 9 N continued to decrease and finally stabilized in the region. Usually, the OCP value at the friction stage reflects the passivation response of the sample after the passive film on the sample surface was quickly mechanically removed [56]. Due to strong passivation ability, the OCP of samples under loads of 1 N and 5 N showed an increasing trend at the initial stage. But as the load was 9 N, the mechanical interaction seemed to exclude re-passivation, therefore the measured potential remained at a low value as long as there is sliding. Further, the corrosion product was continuously being removed by mechanical action during the coupled process of friction and corrosion, so that the fresh metal surface was continuously exposed to the electrolyte, and the anodic dissolution dominated by Cl^- gradually accelerated, resulted in a decrease in OCP value. The characteristics of the wear surface deteriorated as the load increased, thus more wear debris and corrosion pits were generated, thereby promoting the rate of corrosion reaction. Therefore, with the increase of load, the open circuit potential in the friction stage decreased.

The coefficient of friction (COF) of samples showed a first rising and then falling fact, the COF value decreased with the increase of load. During the friction-corrosion process, the protective oxide film on the metal surface is continuously destroyed, and the corrosion is continuously intensified, so that the friction coefficient is continuously reduced [57]. As the load increased, the contact surface was subjected to greater pressure, a higher load led to an increase of plastic deformation on the surface, and higher local work hardening reduced the tendency of adhesive wear. As a result, the mechanical interlocking effect on the sample surface became smoother, thereby reducing the friction coefficient. In addition, the in-situ sample entered a stable trend earlier than the pre-alloyed sample, especially under 5 N and 9 N loads. This is because in-situ samples were usually able to form a stronger oxide film during the friction

process, thus reaching a stable friction coefficient at an earlier time point. The research results of Mischler et al. [58] show that under tribocorrosion conditions, the self-healing property of the alloy oxide film is a key factor in the stability of the friction coefficient. The in-situ samples had stronger corrosion resistance and passive film self-healing ability (consistent with the electrochemical and XPS results mentioned above), so its friction coefficient stabilized earlier.

To further evaluate the tribocorrosion behavior, the PD curve scan was executed during the friction process, as shown in Fig. 10(c, d). The current density of the sample after 0 V increased with the increase of load. The current density of the sample under 9 N load earlier entered a stable state during the scanning process from negative potential to positive potential. Further combined with the friction coefficient curve, as potential changes from negative to positive, the surface of the sample gradually passivated and corroded. Gradually, the COF of the sample decreased and finally tended to be stable due to the gradual generation of corrosion products. Lastly, Fig. 10(e-f) showed the tribocorrosion behavior of samples at CP conditions. Since the cathode potential inhibited the corrosion behavior of the alloy, the sample surface was only affected by mechanical wear in the NaCl solution [59]. The COF of samples slowly decreased as the friction progressed and eventually stabilized.

In summary, the wear rates of samples under various conditions were shown in Fig. 10(g). The samples at CP condition had the smallest wear rate because the electrochemical corrosion was suppressed by cathode reduction. Under OCP conditions, the corrosion products on the scratches were continuously removed by mechanical action during grinding ball reciprocating sliding, so that the fresh metal surface was continuously exposed to the electrolyte, and the wear rate was higher than pure mechanical wear. Lastly, the samples under pd conditions had the largest tribocorrosion wear rate due to accelerated electrochemical corrosion. In addition, under different loads and different electrochemical conditions, In-situ has the smallest wear rate. The wear-corrosion mechanism and the interaction reason between the wear and corrosion of CoCrNi samples will be described in detail in the next section.

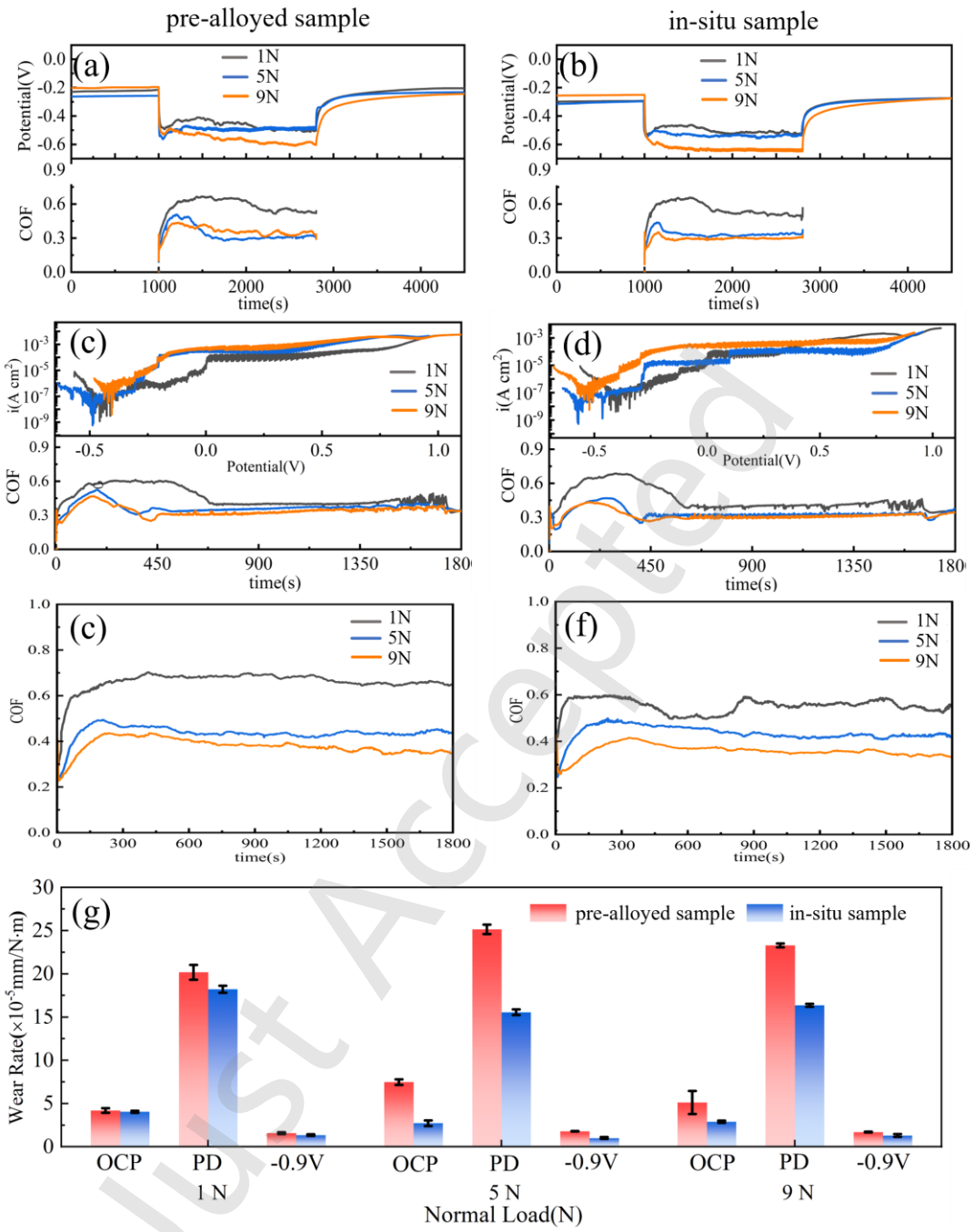

Fig. 10 The tribocorrosion results of different samples: (a, b) the tribocorrosion under OCP conditions; (c, d) the tribocorrosion under PD conditions; (e, f) the tribocorrosion under -0.9 V conditions; (g) the wear rate of in-situ and pre-alloyed samples.

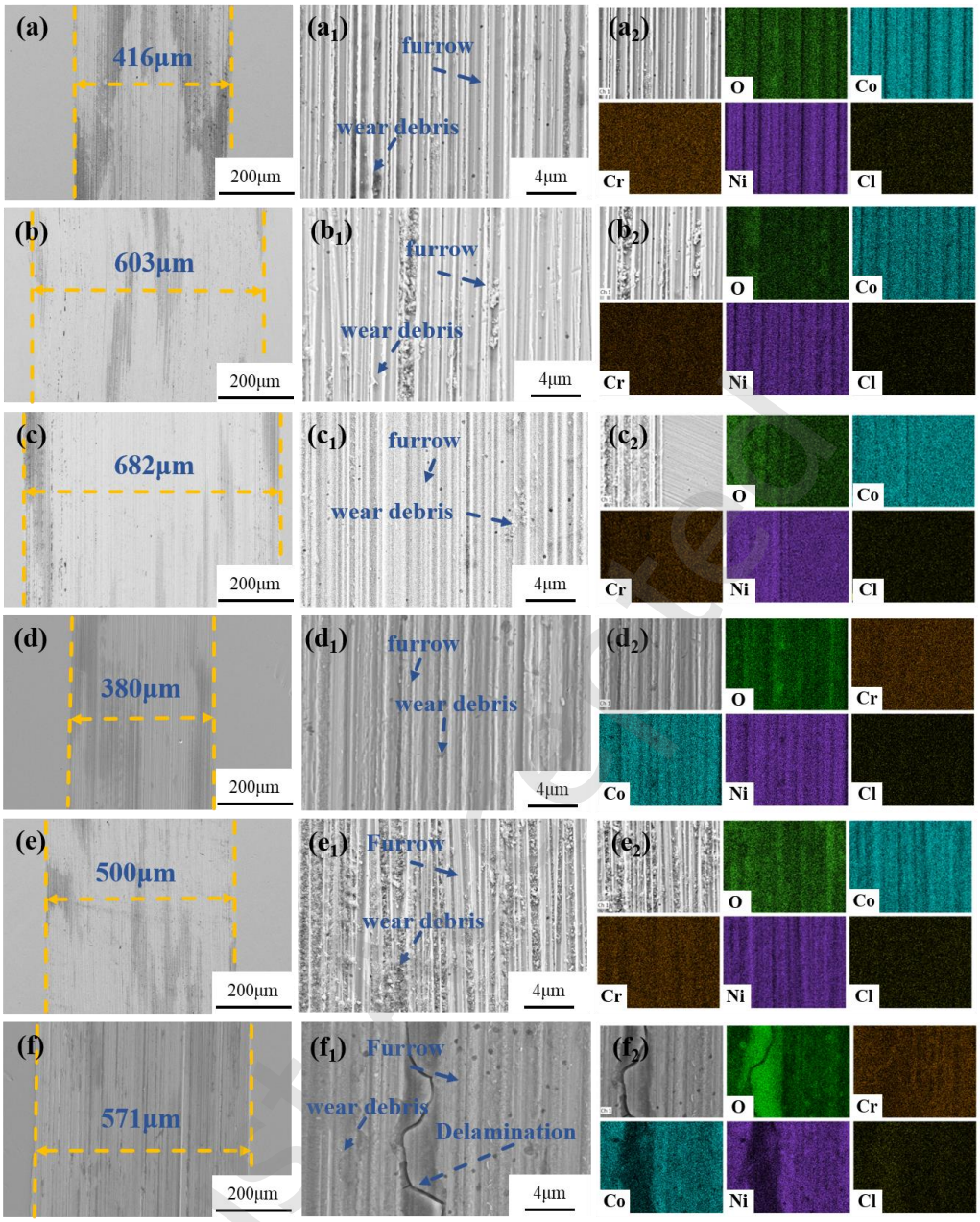

Fig. 11 The morphology of wear tracks on (a-c) pre-alloyed samples and (d-f) in-situ samples at a load of 5 N: (a, d) at CP condition; (b, e) at OCP condition; (c, f) at PD condition.

Fig. 11 showed the SEM image and EDS results of the wear track under load of 5 N. The wear track width of the in-situ sample was smaller than that of pre-alloyed samples under various conditions. In addition, the sample under CP conditions had the smallest wear track width due to pure mechanical wear. However, since there was no external negative potential to inhibit corrosion, the passive film on the sample surface was destroyed during the friction process, and the samples under OCP conditions corroded

with the action of Cl^-, so the wear track width was further increased. Further, as the potential was scanned from negative to positive at PD conditions, the dissolution corrosion intensified [60]. The synergistic effect between corrosion and wear ultimately led to largest wear track width. The wear track surface had typical plowing groove characteristics, and the local shallow plowing marks indicated slight abrasive wear, which should be caused by the plowing effect of the detached wear debris [61]. The wear mechanism of samples under different conditions was typical abrasive wear.

3.4 Synergistic effects between corrosion and wear

Table 2. The summary of various wear volume components for CoCrNi alloy after tribocorrosion.

sample	pre-alloyed samples			in-situ samples		
	1N	5N	9N	1N	5N	9N
T mm^3	9.044E-04	8.075E-03	9.929E-03	8.744E-04	2.941E-03	5.617E-03
W mm^3	8.766E-04	8.048E-03	9.749E-03	8.365E-04	2.902E-03	5.474E-03
W_0 mm^3	3.378E-04	1.928E-03	3.300E-03	2.921E-04	1.082E-03	2.516E-03
W_C mm^3	5.388E-04	6.120E-03	6.449E-03	5.445E-04	1.820E-03	2.958E-03
C mm^3	2.783E-05	2.711E-05	1.805E-04	3.783E-05	3.916E-05	1.425E-04
C_0 mm^3	1.908E-06	1.908E-06	1.908E-06	1.964E-06	1.964E-06	1.964E-06
C_W mm^3	2.592E-05	2.520E-05	1.786E-04	3.587E-05	3.719E-05	1.406E-04
S mm^3	5.647E-04	6.145E-03	6.627E-03	5.803E-04	1.857E-03	3.099E-03
S/T %	62.440	76.103	66.746	66.371	63.142	55.173
C/W %	0.03175	0.00337	0.01852	0.04523	0.01349	0.02604

Firstly, the comparison of pure wear and the effect of wear on corrosion for the samples was conducted. The in-situ sample exhibited a 37% lower mechanical wear volume (W_0)

under various loads. Given that the pre-alloyed and in-situ samples possess similar microstructures and compositions, the classical Archard wear equation (Equation 15) was applied. Since the wear rate is inversely proportional to material hardness, the In-situ sample exhibited a lower pure mechanical wear volume due to higher hardness. Further, the in-situ samples exhibited a higher pure corrosion loss than the pre-alloyed samples, which was aligned with I_{corr} in table S1.

$$V = \frac{KWL}{H} \tag{10}$$

Where V was wear volume, K was wear coefficient, W denoted applied normal load, L was sliding distance, and H was the material hardness.

Further, interaction between wear and corrosion was performed. The wear loss caused by corrosion (W_C) of in-situ samples was 40% lower than that of pre-alloyed samples, except under 1 N load. Which was attributed to the in-situ sample formed a denser passive film, and stabilized the surface condition during reciprocating mechanical scratching and thereby mitigated corrosion-induced wear acceleration. At low loads, the OCP of the pre-alloyed samples required a longer stabilization time compared to the in-situ sample (as shown in Fig. 10(a, b)), led to an unstable surface state that resulted in increased corrosion-induced wear under the 1 N load. Additionally, the wear-intensified corrosion loss (C_W) was evaluated. Since the corrosion resistance of the in-situ sample was lower than the pre-alloyed samples, the C_W of the in-situ sample after mechanical reciprocating scratching was 40% higher than that of the pre-alloyed sample, except under a 9 N load. This was because high mechanical interactions inhibited re-passivation, continuously exposed fresh metal surfaces to the electrolyte, which led to an accelerated anodic dissolution dominated by Cl^- ions, lowering OCP and making C_W the primary mechanism of failure.

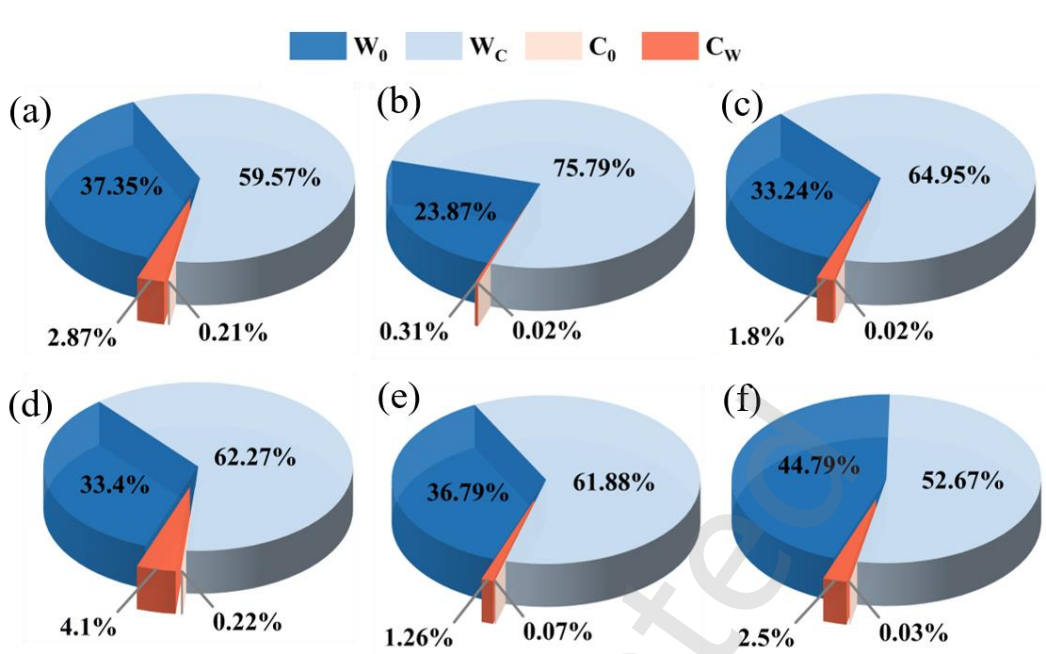

Fig. 12 The summary of various wear volume components for (a-c) pre-alloyed samples and (d-f) in-situ samples after tribocorrosion: (a, d) 1 N load; (b, e) 5 N load; (c, f) 9 N load.

Lastly, by calculating the additional loss of tribocorrosion interaction(*S*), it was found that the *S* of pre-alloyed samples exhibited values twice those of the in-situ sample. However, the values of both samples were Close at the load of 1 N, indicating that load increased the additional loss caused by friction-corrosion interaction. Higher loads increase contact pressure and plastic deformation, prompting the passive film to be mechanically removed more frequently and to a greater depth [62]. For all samples, $C/W \leqslant 0.1$, the in-situ sample exhibited 31% higher *C/W* values than the pre-alloyed sample. These results suggest that wear loss wear was the dominant reason for material loss, and in-situ samples experienced lower wear loss than pre-alloyed samples. Wear accelerates material degradation by removing corrosion products or protective layers that form on top of the material and exposing the bare material to a corrosive environment [63]. Kotlyar et al. [64] found that even when the effect of corrosion is small, the synergistic effect between wear and corrosion is quite significant.

In conclusion, the L-DED CoCrNi alloy experienced primarily wear loss during tribocorrosion (Fig. 12), with corrosion-intensified wear loss due to the reciprocating damage of passive film playing a key role. The in-situ sample exhibited a higher

corrosion current density during tribocorrosion, led to higher C_W. Moreover, the load intensified the material loss of interactions between wear and corrosion. Ultimately, the in-situ sample demonstrated superior mechanical properties, contributed to its enhanced tribocorrosion resistance.

4 discussions

Due to the difference in melting points (Co: 1495 °C, Cr: 1907 °C, Ni: 1455 °C), an inhomogeneous melting process and inhomogeneous molten liquid phase distribution will occur during the L-DED process. As a result, a local concentration gradient will be generated inside the molten pool, which will lead to enhanced Marangoni convection and more intense molten pool flow [65]. The complex molten pool flow disrupted the stable cell growth, increased the transformation from columnar to equiaxed cells during solidification on in-situ samples, thus there were more equiaxed cells existed in in-situ samples than pre-alloyed samples (Fig. 13(a-b)). However, the pre-alloyed samples have a uniform distribution of elements, a more stable molten pool flow, and a slower cooling rate, resulted in the solute elements having enough time to diffuse. The cell boundaries are less affected by the composition segregation and become smoother. The cell boundaries of pre-alloyed samples become thicker due to the enrichment of Cr and Ni (Fig. 4).

In addition, due to liquid phase separation, the solute concentration in local areas is uneven, resulting in a higher solid solution strengthening effect in some areas. Although the overall composition uniformity is poor, the segregation area at the microscale led to local strengthening. To explore this compositional inhomogeneity phenomenon, a 100 μm elemental composition concentration line scan was performed on the sample surface by using EPMA (Fig. 13(c, f)). The element distribution on the surface of the In-situ sample was more uneven. In addition, the nanoscale particle precipitates (Fig. 6) present in the in-situ samples hindered the dislocation movement. Finally, the sample had a higher microhardness.

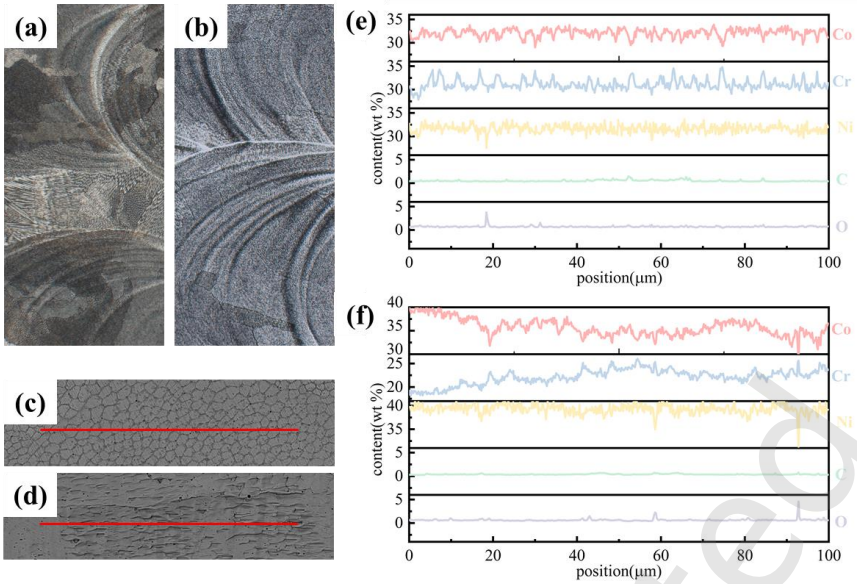

Fig. 13 The microstructure of (a, c, e) pre-alloyed samples and (b, d, f) in-situ samples: (a, b) OM image; (c-f) EPMA line scan.

As shown in Fig. 14, due to the Cr, Ni content of In-situ samples was higher than that of pre-alloyed samples, thus the passive film of in-situ samples had a higher $Cr_2O_3/Cr(OH)_3$ ratio, higher R_{ct}, and a lower I_{pass}. However, the uneven phenomenon resulted in different corrosion trends between different regions, and the uneven phenomenon aggravated the corrosion process. Therefore, in the accelerated corrosion stage after the passive film was broken, the in-situ sample had a relatively uneven structure, and the corrosion rate was higher than that of pre-alloyed samples. Finally, the excellent anti-corrosion of CoCrNi alloy resulted in the loss in the tribocorrosion process mainly being wear loss, thus the in-situ samples had better tribocorrosion resistance due to their superior mechanical properties.

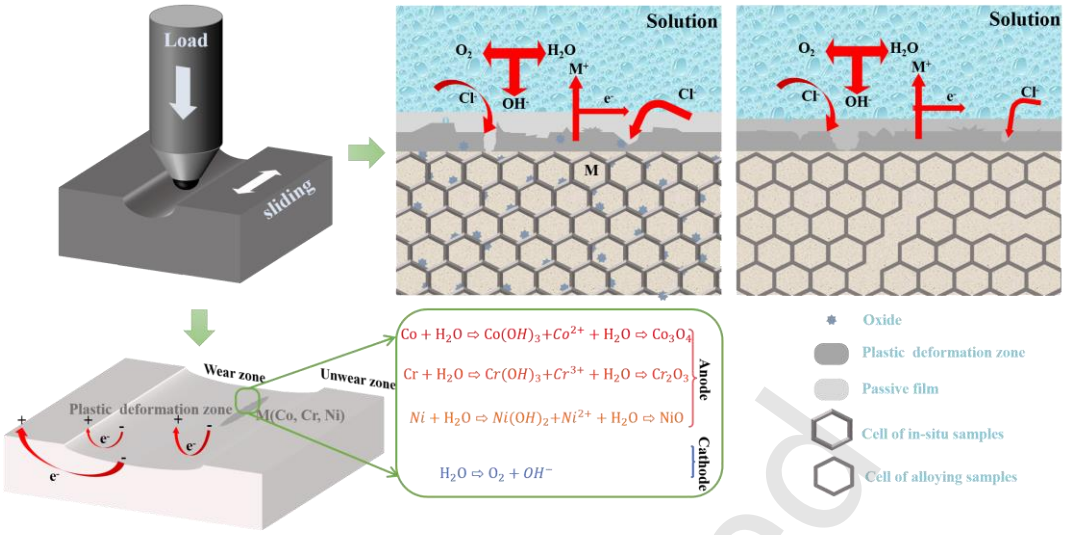

Fig. 14 Schematic of tribocorrosion mechanism on L-DED CoCrNi samples.

5 Conclusion

In this paper, CoCrNi alloy was successfully prepared by using pre-alloyed powder and in-situ powder, and the influence of in-situ alloying on microstructure, corrosion performance, and tribocorrosion behavior was discussed. The synergistic effect between wear and corrosion was quantitatively calculated.

(1) Owing to the in-situ powder promoted the transformation from columnar to equiaxed during solidification, the in-situ samples had finer cells while pre-alloyed samples had finer and more irregular grains.

(2) Solid solution strengthening and nano-precipitation strengthening led to higher microhardness of in-situ samples.

(3) The in-situ CoCrNi samples had a higher $Cr_2O_3/Cr(OH)_3$ ratio, higher R_{ct}, and a lower I_{pass}, indicated a denser and more protective passive film.

(4) The samples were mainly wear loss during tribocorrosion, with W_C playing the main form. The in-situ sample exhibited a higher C_W due to uneven structure. And the load intensified the material loss of interactions between wear and corrosion. The in-situ sample demonstrated superior tribocorrosion resistance.

Availability of data and materials

The raw/processed data required to reproduce these findings cannot be shared at this time as the data also forms part of an ongoing study.

Competing interests

The authors have no competing interests to declare that are relevant to the content of this article.

Acknowledgements

This work was financially supported by the National Science Fund for Distinguished Young Scholars of China (Grant No. 52325503), the Strategic Priority Research Program of the Chinese Academy of Sciences (Grant No. XDB1210402), the National Natural Science Foundation of China (52175168), Guangdong Basic and Applied Basic Research Foundation (2023A1515240006, 2024A1515010452), the Open Fund Project of the Key Laboratory of Advanced Marine Materials (2024K03), Advanced Materials-National Science and Technology Major Project(2025ZD0610300&2025ZD0610301).

CRediT authorship contribution statement

Yudong An: Writing – original draft, Methodology, Investigation, Formal analysis, Data curation. Sufeng Hua: Investigation, Writing – review & editing, Funding acquisition. Jianfang Sun: Investigation, Funding acquisition. Jibin Pu: Methodology, Investigation, Formal analysis, Writing – review & editing, Project administration, Methodology, Investigation, Formal analysis, Data curation, Conceptualization, Funding acquisition.

References:

[1] S. Cao, S. Mischler, Modeling tribocorrosion of passive metals – A review, Current Opinion in Solid State and Materials Science 22 (2018) 127–141. https://doi.org/10.1016/j.cossms.2018.06.001.

[2] D. Landolt, S. Mischler, M. Stemp, Electrochemical methods in tribocorrosion: a critical appraisal, Electrochimica Acta 46 (2001) 3913–3929. https://doi.org/10.1016/S0013-4686(01)00679-X.

[3] L. Fangpo, L. Yonggang, W. Xinhu, L. Caihong, Failure analysis of Ø127mm IEU G105 drill pipe wash out, Engineering Failure Analysis 18 (2011) 1867 – 1872. https://doi.org/10.1016/j.engfailanal.2011.06.018.

[4] S. Mischler, A. Spiegel, D. Landolt, The role of passive oxide films on the degradation of steel in tribocorrosion systems, Wear 225–229 (1999) 1078–1087. https://doi.org/10.1016/S0043-1648(99)00056-3.

[5] X. Yang, R. Zeng, X. Fu, X. Wang, J. Zhou, L. Yu, Influence of the Cu content on the electrochemical corrosion performances of Ni60 coating, Corrosion Science 205 (2022) 110408. https://doi.org/10.1016/j.corsci.2022.110408.

[6] J. Li, B. Lin, H. Zheng, Y. Wang, H. Zhang, Y. Zhang, Z. Nie, J. Tang, Study on pitting corrosion behavior and semi in-situ pitting corrosion growth model of 304 L SS with elastic stress in NaCl corrosion environment, Corrosion Science 211 (2023) 110862. https://doi.org/10.1016/j.corsci.2022.110862.

[7] A. Drach, I. Tsukrov, J. DeCew, J. Aufrecht, A. Grohbauer, U. Hofmann, Field studies of corrosion behaviour of copper alloys in natural seawater, Corrosion Science 76 (2013) 453–464. https://doi.org/10.1016/j.corsci.2013.07.019.

[8] J.-W. Yeh, S.-K. Chen, S.-J. Lin, J.-Y. Gan, T.-S. Chin, T.-T. Shun, C.-H. Tsau, S.-Y. Chang, Nanostructured High-Entropy Alloys with Multiple Principal Elements: Novel Alloy Design Concepts and Outcomes, Advanced Engineering Materials 6 (2004) 299–303. https://doi.org/10.1002/adem.200300567.

[9] X. Yan, Y. Zou, Y. Zhang, Properties and processing technologies of high-entropy alloys, Mater. Futures 1 (2022) 022002. https://doi.org/10.1088/2752-5724/ac5e0c.

[10] T. Li, D. Wang, S. Zhang, J. Wang, Corrosion Behavior of High Entropy Alloys and Their Application in the Nuclear Industry—An Overview, Metals 13 (2023) 363. https://doi.org/10.3390/met13020363.

[11] B. Gludovatz, A. Hohenwarter, K.V.S. Thurston, H. Bei, Z. Wu, E.P. George, R.O. Ritchie, Exceptional damage-tolerance of a medium-entropy alloy CrCoNi at cryogenic temperatures, Nat Commun 7 (2016) 10602. https://doi.org/10.1038/ncomms10602.

[12] R. Zhang, S. Zhao, J. Ding, Y. Chong, T. Jia, C. Ophus, M. Asta, R.O. Ritchie, A.M. Minor, Short-range order and its impact on the CrCoNi medium-entropy alloy, Nature 581 (2020) 283–287. https://doi.org/10.1038/s41586-020-2275-z.

[13] C.K. Soundararajan, H. Luo, D. Raabe, Z. Li, Hydrogen resistance of a 1 GPa strong equiatomic CoCrNi medium entropy alloy, Corrosion Science 167 (2020) 108510. https://doi.org/10.1016/j.corsci.2020.108510.

[14] M.P. Agustianingrum, U. Lee, N. Park, High-temperature oxidation behaviour of CoCrNi medium-entropy alloy, Corrosion Science 173 (2020) 108755. https://doi.org/10.1016/j.corsci.2020.108755.

[15] Y. Ren, Q. Zhou, D. Hua, Z. Huang, Y. Li, Q. Jia, P. Gumbsch, C. Greiner, H. Wang, W. Liu, Wear-resistant CoCrNi multi-principal element alloy at cryogenic temperature, Science Bulletin 69 (2024) 227–236. https://doi.org/10.1016/j.scib.2023.12.003.

[16] X. Zhang, B. Wan, L. Ding, C. Wang, X. Lei, Y. Weng, Z. Jia, Effect of Al and Nb addition on the precipitation hardening and deformation mechanism of CoCrNi medium entropy alloy, Journal of Alloys and Compounds 992 (2024) 174619. https://doi.org/10.1016/j.jallcom.2024.174619.

[17] Y. Dong, Y. Zhang, J. Yu, S. Qin, H. Zhang, Z. Yang, T. Hu, X. Zhang, Z. Ren, Enhanced high-temperature oxidation resistance and corrosion resistance of NiCoCr medium-entropy alloys by interstitial N-doping, Journal of Alloys and Compounds 1040 (2025) 183493. https://doi.org/10.1016/j.jallcom.2025.183493.

[18] M. Yi, J. Tu, L. Yang, Z. Zhou, S. Chen, L. Ding, Y. Du, Y. Qiu, Y. Liang, Microstructural mechanisms endowing high strength-ductility synergy in CoCrNi medium entropy alloy prepared by laser powder bed fusion, Addit. Manuf. 87 (2024) 104229. https://doi.org/10.1016/j.addma.2024.104229.

[19] P. Ma, Y. Peng, J. Hu, Y. Yu, Y. Liu, M. Chen, J. Qiu, Microstructure, mechanical and electrochemical performance of spark plasma sintered CoCrNi medium-entropy alloy, Journal of Alloys and Compounds 1007 (2024) 176321. https://doi.org/10.1016/j.jallcom.2024.176321.

[20] Q. Chao, T. Guo, T. Jarvis, X. Wu, P. Hodgson, D. Fabijanic, Direct laser deposition cladding

of AlxCoCrFeNi high entropy alloys on a high-temperature stainless steel, Surface and Coatings Technology 332 (2017) 440–451. https://doi.org/10.1016/j.surfcoat.2017.09.072.

[21] I. Kunce, M. Polanski, J. Bystrzycki, Microstructure and hydrogen storage properties of a TiZrNbMoV high entropy alloy synthesized using Laser Engineered Net Shaping (LENS), International Journal of Hydrogen Energy 39 (2014) 9904–9910. https://doi.org/10.1016/j.ijhydene.2014.02.067.

[22] D. Svetlizky, M. Das, B. Zheng, A.L. Vyatskikh, S. Bose, A. Bandyopadhyay, J.M. Schoenung, E.J. Lavernia, N. Eliaz, Directed energy deposition (DED) additive manufacturing: Physical characteristics, defects, challenges and applications, Materials Today 49 (2021) 271–295. https://doi.org/10.1016/j.mattod.2021.03.020.

[23] A. Ostovari Moghaddam, N.A. Shaburova, M.N. Samodurova, A. Abdollahzadeh, E.A. Trofimov, Additive manufacturing of high entropy alloys: A practical review, Journal of Materials Science & Technology 77 (2021) 131–162. https://doi.org/10.1016/j.jmst.2020.11.029.

[24] A. Amar, M. Wang, L. Zhang, J. Li, L. Huang, H. Yan, Y. Zhang, Y. Lu, Additive manufacturing of VCoNi medium-entropy alloy: Microstructure evolution and mechanical properties, Addit. Manuf. 68 (2023) 103522. https://doi.org/10.1016/j.addma.2023.103522.

[25] M. Zheng, C. Li, X. Zhang, Z. Ye, X. Yang, J. Gu, The influence of columnar to equiaxed transition on deformation behavior of FeCoCrNiMn high entropy alloy fabricated by laser-based directed energy deposition, Addit. Manuf. 37 (2021) 101660. https://doi.org/10.1016/j.addma.2020.101660.

[26] M.A. Melia, J.D. Carroll, S.R. Whetten, S.N. Esmaeely, J. Locke, E. White, I. Anderson, M. Chandross, J.R. Michael, N. Argibay, E.J. Schindelholz, A.B. Kustas, Mechanical and Corrosion Properties of Additively Manufactured CoCrFeMnNi High Entropy Alloy, Addit. Manuf. 29 (2019) 100833. https://doi.org/10.1016/j.addma.2019.100833.

[27] B. Meier, F. Warchomicka, J. Petrusa, P. Angerer, J. Wosik, R. Kaindl, V. Petrovic, W. Waldhauser, C. Sommitsch, Influence of powder production process and properties on material properties of Ti6Al4V manufactured by L-PBF, Int J Adv Manuf Technol 123 (2022) 1577–1588. https://doi.org/10.1007/s00170-022-10250-y.

[28] C. Pleass, S. Jothi, Influence of powder characteristics and additive manufacturing process parameters on the microstructure and mechanical behaviour of Inconel 625 fabricated by Selective Laser Melting, Additive Manufacturing 24 (2018) 419–431. https://doi.org/10.1016/j.addma.2018.09.023.

[29] C. Weiss, J. Heslenfeld, J.K. Saewe, S. Bremen, C.L. Häfner, Investigation on the influence of powder humidity in Laser Powder Bed Fusion (LPBF), Procedia CIRP 111 (2022) 115–120. https://doi.org/10.1016/j.procir.2022.08.102.

[30] S.E. Brika, M. Letenneur, C.A. Dion, V. Brailovski, Influence of particle morphology and size distribution on the powder flowability and laser powder bed fusion manufacturability of Ti-6Al-4V alloy, Additive Manufacturing 31 (2020) 100929. https://doi.org/10.1016/j.addma.2019.100929.

[31] L. Lan, Z. Yang, W. Wang, Z. Cui, X. Hao, Effect of initial powder particle size on densification behavior and mechanical properties of laser additive manufacturing of AlCoCrFeNi2.1 eutectic high-entropy alloy, Powder Technology 420 (2023) 118379. https://doi.org/10.1016/j.powtec.2023.118379.

[32] S. Ziri, A. Hor, C. Mabru, Combined effect of powder properties and process parameters on the density of 316L stainless steel obtained by laser powder bed fusion, Int J Adv Manuf Technol 120 (2022) 6187–6204. https://doi.org/10.1007/s00170-022-09160-w.

[33] L. Haferkamp, L. Haudenschild, A. Spierings, K. Wegener, K. Riener, S. Ziegelmeier, G.J. Leichtfried, The Influence of Particle Shape, Powder Flowability, and Powder Layer Density on Part Density in Laser Powder Bed Fusion, Metals 11 (2021) 418. https://doi.org/10.3390/met11030418.

[34] M.H. Mosallanejad, B. Niroumand, A. Aversa, A. Saboori, In-situ alloying in laser-based additive manufacturing processes: A critical review, Journal of Alloys and Compounds 872 (2021) 159567. https://doi.org/10.1016/j.jallcom.2021.159567.

[35] P. Ren, H. Meng, Q. Xia, Z. Zhu, M. He, Influence of seawater depth and electrode potential on the tribocorrosion of Ti6Al4V alloy under the simulated deep-sea environment by in-situ electrochemical technique, Corrosion Science 180 (2021) 109185. https://doi.org/10.1016/j.corsci.2020.109185.

[36] Z. Wang, Y. Yan, Y. Wu, X. Huang, Y. Zhang, Y. Su, L. Qiao, Corrosion and tribocorrosion behavior of equiatomic refractory medium entropy TiZr(Hf, Ta, Nb) alloys in chloride solutions, Corrosion Science 199 (2022) 110166. https://doi.org/10.1016/j.corsci.2022.110166.

[37] Thermodynamics and Theory of External and Internal Oxidation of Alloys, (2010) 180–194. https://doi.org/10.1016/B978-044452787-5.00012-3.

[38] M. Li, Y. Qiu, N. Birbilis, A. Taylor, R.K.W. Marceau, C. Zhang, Y. Yan, J. Liu, On the corrosion of a nano-oxide dispersion strengthened CoCrNi medium entropy alloy prepared by laser powder bed fusion, Corrosion Science 257 (2025) 113341. https://doi.org/10.1016/j.corsci.2025.113341.

[39] S.K. Guo, Z.L. Ma, G.H. Xia, X.Y. Li, Z.Q. Xu, W.Z. Li, X.Y. Jin, X.W. Cheng, Pursuing ultrastrong and ductile medium entropy alloys via architecting nanoprecipitates-enhanced hierarchical heterostructure, Acta Materialia 263 (2024) 119492. https://doi.org/10.1016/j.actamat.2023.119492.

[40] C.A. Della Rovere, J.H. Alano, R. Silva, P.A.P. Nascente, J. Otubo, S.E. Kuri, Characterization of passive films on shape memory stainless steels, Corrosion Science 57 (2012) 154–161. https://doi.org/10.1016/j.corsci.2011.12.022.

[41] N.S. McIntyre, D.D. Johnston, L.L. Coatsworth, R.D. Davidson, J.R. Brown, X-ray photoelectron spectroscopic studies of thin film oxides of cobalt and molybdenum, Surface and Interface Analysis 15 (1990) 265–272. https://doi.org/10.1002/sia.740150406.

[42] T.J. Chuang, C.R. Brundle, D.W. Rice, Interpretation of the x-ray photoemission spectra of cobalt oxides and cobalt oxide surfaces, Surface Science 59 (1976) 413–429. https://doi.org/10.1016/0039-6028(76)90026-1.

[43] A.M. Venezia, R. Bertoncello, G. Deganello, X-ray photoelectron spectroscopy investigation of pumice-supported nickel catalysts, Surface and Interface Analysis 23 (1995) 239–247. https://doi.org/10.1002/sia.740230408.

[44] P. Dolle, M. Alnot, J.J. Ehrhardt, A. Cassuto, Etude par spectroscopie de photoelectrons et d'electrons auger des etapes initiales de l'oxydation du chrome polycristallin, Journal of Electron Spectroscopy and Related Phenomena 17 (1979) 299–321. https://doi.org/10.1016/0368-2048(79)80007-9.

[45] W.-Y. Howng, R.J. Thorn, Investigation of the electronic structure of *La*1−x(*M*2+)x*CrO*3, *Cr*2*O*3 and La2O3 by X-ray photoelectron spectroscopy, Journal of Physics and Chemistry of Solids 41 (1980) 75–81. https://doi.org/10.1016/0022-3697(80)90123-7.

[46] T.P. Moffat, R.M. Latanision, R.R. Ruf, An X-ray photoelectron spectroscopy study of chromium-metalloid alloys—III, Electrochimica Acta 40 (1995) 1723–1734. https://doi.org/10.1016/0013-4686(95)00015-7.

[47] J.Y. Zhang, Y.H. Zhou, Z.Q. Ren, J.H. Luan, Y.L. Zhao, T. Yang, The influence of microstructural evolutions on electrochemical corrosion and passive behavior in precipitation-strengthened high-entropy alloys, Corrosion Science 233 (2024) 112074. https://doi.org/10.1016/j.corsci.2024.112074.

[48] C.B. Nascimento, U. Donatus, C.T. Ríos, R.A. Antunes, Electronic properties of the passive films formed on CoCrFeNi and CoCrFeNiAl high entropy alloys in sodium chloride solution, Journal of Materials Research and Technology 9 (2020) 13879–13892. https://doi.org/10.1016/j.jmrt.2020.10.002.

[49] Effect of nitrogen on corrosion behaviour of a novel high nitrogen medium-entropy alloy CrCoNiN manufactured by pressurized metallurgy, Journal of Materials Science & Technology 34 (2018) 1781–1790. https://doi.org/10.1016/j.jmst.2018.03.021.

[50] T. Misawa, K. Hashimoto, S. Shimodaira, The mechanism of formation of iron oxide and oxyhydroxides in aqueous solutions at room temperature, Corrosion Science 14 (1974) 131–149. https://doi.org/10.1016/S0010-938X(74)80051-X.

[51] X. Li, J.D. Henderson, F.P. Filice, D. Zagidulin, M.C. Biesinger, F. Sun, B. Qian, D.W. Shoesmith, J.J. Noël, K. Ogle, The contribution of Cr and Mo to the passivation of Ni22Cr and Ni22Cr10Mo alloys in sulfuric acid, Corrosion Science 176 (2020) 109015. https://doi.org/10.1016/j.corsci.2020.109015.

[52] Y. Wang, S. Song, J. Wang, Y. Behnamian, L. Xu, H. Fan, D.-H. Xia, Correlation between Passivity Breakdown and Composition of Passive Film Formed on Alloy 690 Studied by Sputtering XPS and FIB-HRTEM, J. Electrochem. Soc. 166 (2019) C332. https://doi.org/10.1149/2.1291912jes.

[53] G.-H. Wang, Y.-Q. Jiang, C.-A. Guo, Effect of Nitrogen Content on the Corrosion Resistance of High-nitrogen Austenitic Stainless Steel for Nonmagnetic Drill Collar in a Harsh Service Environment, International Journal of Electrochemical Science 17 (2022) 220656. https://doi.org/10.20964/2022.06.66.

[54] F. Weng, Y. Chew, W.K. Ong, Y. Man, S. Sui, C. Tan, F.L. Ng, M.H. Goh, G. Bi, Enhanced corrosion resistance of laser aided additive manufactured CoCrNi medium entropy alloys with oxide inclusion, Corrosion Science 195 (2022) 109965. https://doi.org/10.1016/j.corsci.2021.109965.

[55] A.C. Vieira, L.A. Rocha, N. Papageorgiou, S. Mischler, Mechanical and electrochemical deterioration mechanisms in the tribocorrosion of Al alloys in NaCl and in NaNO3 solutions, Corrosion Science 54 (2012) 26–35. https://doi.org/10.1016/j.corsci.2011.08.041.

[56] R.C.C. Silva, R.P. Nogueira, I.N. Bastos, Tribocorrosion of UNS S32750 in chloride medium: Effect of the load level, Electrochimica Acta 56 (2011) 8839–8845. https://doi.org/10.1016/j.electacta.2011.07.077.

[57] M. Feyzi, K. Fallahnezhad, M. Taylor, R. Hashemi, The Tribocorrosion Behaviour of Ti-6Al-4 V Alloy: The Role of Both Normal Force and Electrochemical Potential, Tribology Letters

70 (2022). https://doi.org/10.1007/s11249-022-01624-0.

[58] S. Guadalupe Maldonado, S. Mischler, M. Cantoni, W.-J. Chitty, C. Falcand, D. Hertz, Mechanical and chemical mechanisms in the tribocorrosion of a Stellite type alloy, Wear 308 (2013) 213–221. https://doi.org/10.1016/j.wear.2013.04.007.

[59] X.-Z. Wang, Y. Wang, Z. Huang, Q. Zhou, H. Wang, Tribocorrosion Behavior of CoCrNi Medium Entropy Alloy in Simulated Seawater, Metals 12 (2022) 401. https://doi.org/10.3390/met12030401.

[60] Y. Liu, F. Zhang, Z. Huang, Q. Zhou, Y. Ren, Y. Du, H. Wang, Mechanical and dry sliding tribological properties of CoCrNiNbx medium-entropy alloys at room temperature, Tribology International 163 (2021) 107160. https://doi.org/10.1016/j.triboint.2021.107160.

[61] V. Bhardwaj, Q. Zhou, F. Zhang, W. Han, Y. Du, K. Hua, H. Wang, Effect of Al addition on the microstructure, mechanical and wear properties of TiZrNbHf refractory high entropy alloys, Tribology International 160 (2021) 107031. https://doi.org/10.1016/j.triboint.2021.107031.

[62] A. López-Ortega, J.L. Arana, R. Bayón, Tribocorrosion of Passive Materials: A Review on Test Procedures and Standards, International Journal of Corrosion 2018 (2018) 7345346. https://doi.org/10.1155/2018/7345346.

[63] A.W. Batchelor, G.W. Stachowiak, Predicting synergism between corrosion and abrasive wear, Wear 123 (1988) 281–291. https://doi.org/10.1016/0043-1648(88)90144-5.

[64] D. Kotlyar, C.H. Pitt, M.E. Wadsworth, Simultaneous Corrosion and Abrasion Measurements Under Grinding Conditions, CORROSION 44 (1988) 221–228. https://doi.org/10.5006/1.3583929.

[65] M.S. Knieps, W.J. Reynolds, J. Dejaune, A.T. Clare, A. Evirgen, In-situ alloying in powder bed fusion: The role of powder morphology, Materials Science and Engineering: A 807 (2021) 140849. https://doi.org/10.1016/j.msea.2021.140849.